Self-amplified spontaneous emission for a single pass free-electron laser

L. Giannessi,[1,*] D. Alesini,[2] P. Antici,[2] A. Bacci,[2,4] M. Bellaveglia,[2] R. Boni,[2] M. Boscolo,[2] F. Briquez,[10] M. Castellano,[2] L. Catani,[8] E. Chiadroni,[2] A. Cianchi,[8] F. Ciocci,[1] A. Clozza,[2] M. E. Couprie,[10] L. Cultrera,[2] G. Dattoli,[1] M. Del Franco,[1] A. Dipace,[1] G. Di Pirro,[2] A. Doria,[1] A. Drago,[2] W. M. Fawley,[11] M. Ferrario,[2] L. Ficcadenti,[2] D. Filippetto,[2] F. Frassetto,[6] H. P. Freund,[12] V. Fusco,[1,2] G. Gallerano,[1] A. Gallo,[2] G. Gatti,[2] A. Ghigo,[2] E. Giovenale,[1] A. Marinelli,[9,2] M. Labat,[10] B. Marchetti,[8] G. Marcus,[9] C. Marrelli,[2] M. Mattioli,[2] M. Migliorati,[2,5] M. Moreno,[5] A. Mostacci,[5] G. Orlandi,[13] E. Pace,[2] L. Palumbo,[2,5] A. Petralia,[1] M. Petrarca,[2] V. Petrillo,[3,4] L. Poletto,[6] M. Quattromini,[1] J. V. Rau,[7] S. Reiche,[13] C. Ronsivalle,[1] J. Rosenzweig,[9] A. R. Rossi,[2,4] V. Rossi Albertini,[7] E. Sabia,[1] L. Serafini,[4] M. Serluca,[5] I. Spassovsky,[1] B. Spataro,[2] V. Surrenti,[1] C. Vaccarezza,[2] M. Vescovi,[2] and C. Vicario[13]

[1]*ENEA C.R. Frascati, Via E. Fermi 45, 00044 Frascati (RM), Italy*
[2]*INFN-LNF, Via E. Fermi 40, 00044 Frascati, RM, Italy*
[3]*Università degli Studi di Milano, Via Celoria 16, 20133 Milano, Italy*
[4]*INFN-Mi,Via Celoria 16, 20133 Milano, Italy*
[5]*Università La Sapienza, Piazzale Aldo Moro 1, 00185 Roma, Italy*
[6]*CNR-IFN, Via Trasea 7, 35131 Padova, Italy*
[7]*ISM-CNR Via del Fosso del Cavaliere 100, 00133 Roma, Italy*
[8]*INFN-Roma II, Via della Ricerca Scientifica 1, 00133 RM, Italy*
[9]*UCLA, 405 Hilgard Avenue, Los Angeles, California 90095-1547, USA*
[10]*SOLEIL, L'Orme des Merisiers Saint-Aubin, BP 48 91192 GIF-sur-Yvette Cedex, France*
[11]*Sincrotrone Trieste S.C.p.A., Area Science Park, S.S. 14 Km 163.5, I-34149 Trieste, Italy*
[12]*Science Applications International Corporation, McLean, Virginia 22102, USA*
[13]*Paul Scherrer Institute, 5232 Villigen, PSI, Switzerland*

(Received 24 February 2011; published 29 June 2011)

SPARC (acronym of ''Sorgente Pulsata ed Amplificata di Radiazione Coerente'', i.e. *Pulsed and Amplified Source of Coherent Radiation*) is a single pass free-electron laser designed to obtain high gain amplification at a radiation wavelength of 500 nm. Self-amplified spontaneous emission has been observed driving the amplifier with the high-brightness beam of the SPARC linac. We report measurements of energy, spectra, and exponential gain. Experimental results are compared with simulations from several numerical codes.

DOI: 10.1103/PhysRevSTAB.14.060712 PACS numbers: 41.60.Cr, 41.50.+h, 42.55.Vc

I. INTRODUCTION

Recent progress in accelerator technology has led to wide-range tunable laser radiation in the vacuum-ultraviolet and x-ray spectral regions by means of the development of free-electron lasers (FEL) based on the principle of self-amplified spontaneous emission (SASE) [1–5]. In a SASE FEL, lasing occurs in a single pass of a relativistic, high-brightness electron beam driven through a long undulator magnetic structure. SASE emission and its properties in both frequency and time domains have been observed and studied at various wavelengths in several experiments [6–10]. More recently, radiation in the hard x-ray range, at wavelength of 1.5 Å, has been obtained at LCLS [11].

*luca.giannessi@enea.it

SPARC is a single pass FEL amplifier test facility designed to study the amplification process under various operating conditions. A layout of the SPARC FEL is shown in Fig. 1.

The electron beam is generated in a high-brightness rf gun [Fig. 1 (A)], which was implemented in the first operating phase for examining the beam evolution in the drift between the gun and the main linac [12]. The electron beam then enters in a linac composed of three traveling wave-type accelerating sections [Fig. 1 (B) and Fig. 2].

The undulator [Fig. 1 (D) and Fig. 3] consists of six permanent magnet sections with period $\lambda_u = 2.8$ cm. The intersections between the modules host quadrupoles for horizontal focusing and radiation diagnostic stations. Each station is equipped with actuators allowing the insertion of alumina screens to monitor the electron beam size and position, and aluminum mirrors to extract the radiation. At the end of the undulator sequence an in-vacuum spectrometer built by the LUXOR Laboratory (Padova) [13,14] is the main radiation diagnostic.

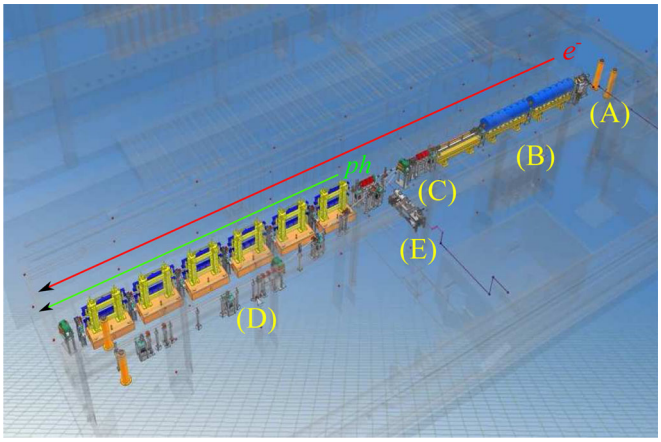

FIG. 1. General SPARC layout. (A) High-brightness rf gun (BNL/UCLA/LCLS design). (B) Linac, composed by three traveling wave-type accelerating sections. (C) Transfer line. (D) Undulator, made by six permanent magnet modules, realized by ACCEL Gmbh. (E) Seeding equipment.

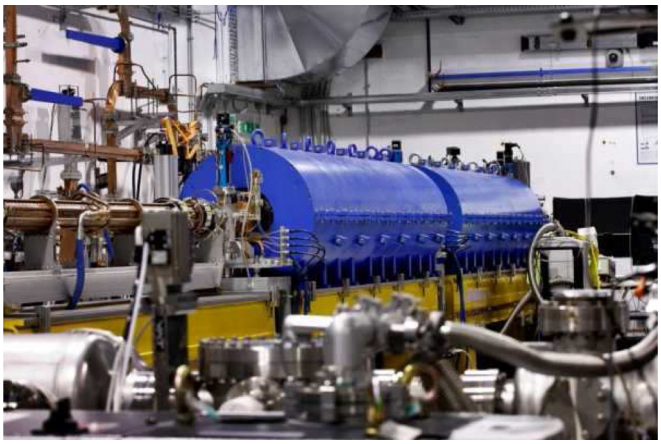

FIG. 2. SPARC linac accelerator provides a final maximum beam energy of about 178 MeV. The first two linac accelerating structures are surrounded by two long solenoids (blue structures) providing the additional focusing (with a maximum field of 0.18 T) required to match the beam envelope to the linac, according to the invariant envelope conditions, when the linac operates in velocity bunching compression mode.

Commissioning of the SPARC FEL began in autumn 2008 with the following main goals: (1) transport the beam through the vacuum chamber up to the beam dump consistently with the matching condition in the undulator; (2) characterization of the spontaneous and stimulated radiation; and (3) demonstration of ''velocity bunching'' techniques [15,16] according to the invariant envelope condition [17]. These steps were completed during winter 2009, and the first SASE FEL spectra were obtained in February of the same year. A few months later, a substantial increase of the brilliance of the radiation extracted from the FEL source was obtained with a longitudinally flattop e-beam current, by increasing the bunch

FIG. 3. SPARC undulator consisting of six sections made by 75 periods of 2.8 cm each (77 periods including two termination periods), with gaps variable in the range from 25 to 8.4 mm (limited by the vacuum chamber) corresponding to a maximum undulator parameter $K_u \sim 2.2$ (see definition below) at the minimum gap.

charge and by anticipating the phase in the gun to reduce the debunching in the first stage of acceleration, permitting a higher beam current. In this paper we report on SPARC lasing performance obtained so far in SASE mode. In the next section we discuss the accelerator performance, the diagnostics, and the characteristics of the electron beam available for the SASE FEL amplification experiment. We then describe in detail the energy calibration of the spectrometer used as the main diagnostic. Finally, we report on observation and analysis of SASE emission at 500 nm.

II. ELECTRON BEAM CHARACTERIZATION

The SPARC beam diagnostic system has been designed to ensure the possibility of optimizing the beam acceleration and matching through all the linac structures and the undulator, and to measure the main beam parameters prior to injection in the FEL. The beam envelope is reconstructed by measuring the rms beam size on four screens along the linac: at the entrance of each rf structure and at the exit of the accelerator, in the seven meter transfer line (TL) leading to the undulator. The TL [Fig. 1 (C)] hosts six quadrupoles arranged in two triplets and is designed to match the beam to undulator optics. Along the transfer line a dipole-based magnetic spectrometer deflects the beam on a Ce:Yag screen 100 μm thick, allowing the measurement of beam energy and energy spread. The first triplet in the TL is used to measure the projected emittance by quadrupole scan [18]. An S-band, 5 cell, standing wave rf deflecting cavity (RFD) [19,20], placed before the dipole, in combination with the first quadrupole triplet and the dipole itself, is used to measure the slice longitudinal (bunch length, slice energy spread, longitudinal trace space) and transverse (slice emittance) beam parameters. During

commissioning, the deflecting voltage in the RFD was limited to a maximum of 1.5 MV; this limited the resolution to 50 fs/pixel at 150 MeV. The overall measurement resolution is affected by the beam dimensions on the screen with the RFD switched off. For typical SPARC beam sizes at the screen (70 μm), the calculated resolution is about 90 fs at 150 MeV. Via a similar argument, the resolution of the magnetic spectrometer can be estimated to be 5 keV/pixel at 150 MeV, and the overall measurement resolution on the relative energy spread to be about 0.01%.

The beam used in the SASE FEL experiment was obtained with a longitudinally flattop laser pulse, with a length of 6–8 ps (FWHM). Whereas the cathode can nominally deliver up to 1 nC, the charge extracted in the FEL experiments was about 400 pC. This choice resulted from an optimization of the achievable beam brightness, which was mainly limited by the field gradient at the gun. A higher charge, with the gun operated at a maximum achievable gradient of about 105 MV/m, was accompanied by an increase of the beam emittance without a corresponding increase of the peak current. Magnetic compression has not been implemented at SPARC, while velocity bunching was not considered as an option because of

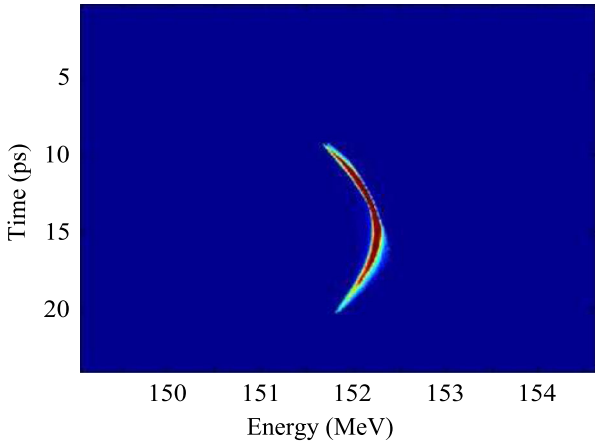

FIG. 4. Phase space of the e-beam measured with time/energy dispersion induced by rf-deflector/spectrometer dipole.

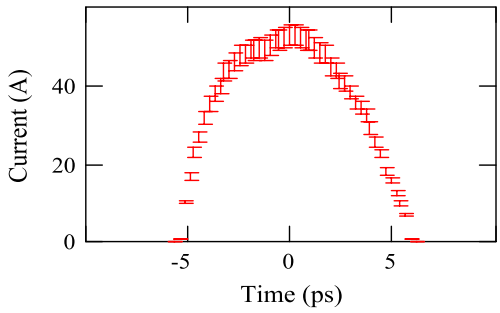

FIG. 5. Beam current as a function of time along the microbunch. Error bars represent ±1 standard deviation evaluated by combining quadratically the relative local uncertainties on charge and bunch length (~ 5%).

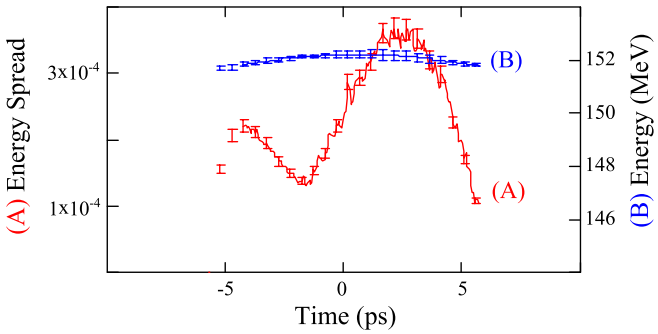

FIG. 6. Beam energy spread (A) and beam energy (B) as a function of time along the bunch. Error bars represent ±1 standard deviation on the local energy spread measure. The energy error bars are calculated as ±3 standard deviations of the energy measured at the specific longitudinal position. This parameter is related to the instrumental accuracy of the single shot measurement and does not reflect shot to shot energy fluctuations or drifts as indicated in Table I.

the consistent drop in the beam energy and of the large energy spread induced at the end of the acceleration phase, when operating the first linac section off crest. A typical reconstructed longitudinal phase space is shown in Fig. 4.

We measured an energy spread of the order of 0.1% and an energy stability better than 0.1%. In Fig. 5 the beam current along the electron bunch, deduced by the phase space of Fig. 4, is shown. In this condition the maximum current is about 53 A and the rms bunch length is 2.6 ps. Figure 6 presents the beam energy (blue) and the incoherent energy spread (red) as a function of the position along the bunch. The main parameters of the beam during the experiment are summarized in Table I. The transverse emittance measured with the quadrupole scan at the end of the linac is 2.9(2.5) mm-mrad in the vertical (horizontal) plane.

TABLE I. Main beam parameters measured during the experiment. The error figures represent 1 standard deviation over 20 acquisitions (except for the charge which is obtained with 100 acquisitions). The slice energy spread uncertainty is instead calculated as the standard deviation of the energy spread averaged over the bunch length, in a single shot measurement.

Beam energy (MeV)	152.08–149.8
Relative energy spread (projected, rms)	$9.0 \times 10^{-4} \pm 0.8 \times 10^{-4}$
Relative energy spread (slice, rms)	$2.0 \times 10^{-4} \pm 0.8 \times 10^{-4}$
Bunch length (ps, rms)	2.60 ± 0.05
Electron charge (pC)	400 ± 20
Beam current (A)	53 ± 4
Repetition rate (Hz)	10
Vertical emittance (projected, mm mrad)	2.9 ± 0.3
Horizontal emittance (projected, mm mrad)	2.5 ± 0.3

During a typical eight-hours shift, we observed slow drifts, mainly in the beam energy, in the range listed in the table.

III. RADIATION DIAGNOSTICS

The main diagnostic used to measure the output radiation is an in-vacuum spectrometer [13,14] operating in the spectral range 35–370 nm. The instrument is a 1 m normal incidence spectrometer with a Princeton UV grade CCD camera, allowing the detection of spectra both in single shot and in integrated mode. The CCD camera and the necessary upstream optics were calibrated in energy. The spectral image permits the reconstruction of the total pulse energy together with the spectral parameters as central wavelength, linewidth, and, in the vertical direction, of the spot size and position of the radiation beam.

A layout of the present setup is shown in Fig. 7.

After exiting from the last undulator section, a metallic aluminum mirror deflects the light beam towards the spectrometer. The FEL radiation is P polarized and the theoretical P reflectivity has been used in deriving a calibration factor. Different filters are available along the radiation beam line, mounted on two filter wheels (FW1, FW2). Neutral density filters allow the attenuation of the radiation intensity at the CCD for wavelengths longer than 350 nm. Bandpass filters may be used to remove intense signals from long wavelengths while observing the higher order harmonics of the FEL. All the filters were characterized by a wavelength transmission curve which is used for the energy calibration. At the entrance of the spectrometer, the light passes through a rectangular slit of variable horizontal width (30–2000 μm). Assuming a circular beam at the slit entrance, the energy lost at the slit was recovered as a function of its width by measuring the spot profile in the vertical direction. Calibration curves of the slit attenuation were derived by reconstructing the spot of a fixed source while varying the slit aperture. This procedure was repeated using both the SASE FEL radiation (at 500 nm) and the radiation from the seed laser (at 400 nm) available at SPARC, obtaining similar results. The spectrometer spectral range covers the interval 35–560 nm with three different gratings (600, 1200, 2400 grooves/mm) operating at different wavelengths. The first two gratings are

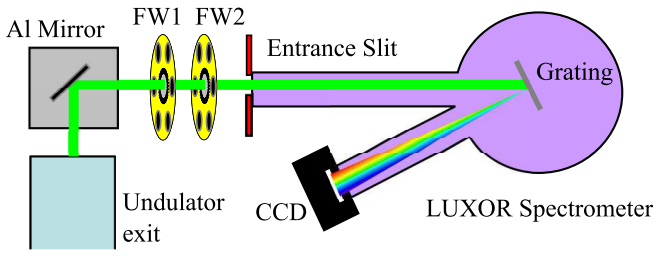

FIG. 7. Layout of the spectrometer and radiation diagnostics at the end of the undulator sequence.

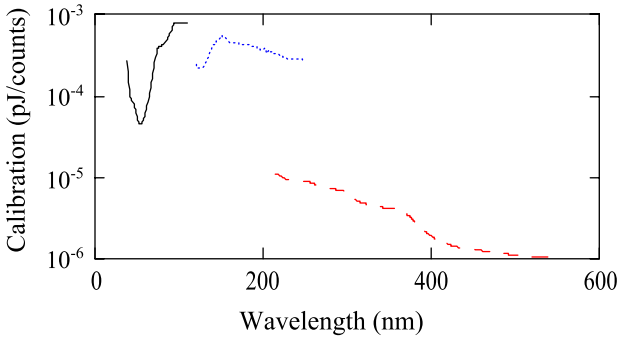

FIG. 8. Energy calibration including the contribution of the CCD detector, the reflectivity of the different gratings. A platinum coated grating (2400 grooves) covers the short wavelength range (black continuous) and two aluminum coated gratings, 1200 grooves (blue dotted) and 600 grooves (red dashed) cover the middle and long wavelength ranges, respectively.

Al/MgF2 coated, while the last is Pt coated. Each grating was characterized by its own efficiency curve. The spectrometer is equipped with a CCD detector (Versarray, 1300B-Princeton Instruments) with a gain of 1.14 e^-/ADU (analog to digital unit). The CCD efficiency (e^-/incident photon) is given by the product of the quantum efficiency (interacting photon/incident photon) and the quantum yield (e^-/interacting photon). The spectrometer efficiency is given by the product of the grating efficiency and the CCD efficiency (see Fig. 8). We have accounted for the device magnification which zooms on the CCD the image of the entrance slit with a magnification factor of 1.374. The global calibration is the product of the calibration curves of all the elements crossed by the light at a given wavelength: last mirror, filters, grating, CCD.

The calibration procedure was tested at 500 nm by comparing the energy reconstructed from the SASE spectra with the direct measurement from a calibrated high sensitivity pyroelectric detector (see Fig. 9). The data set

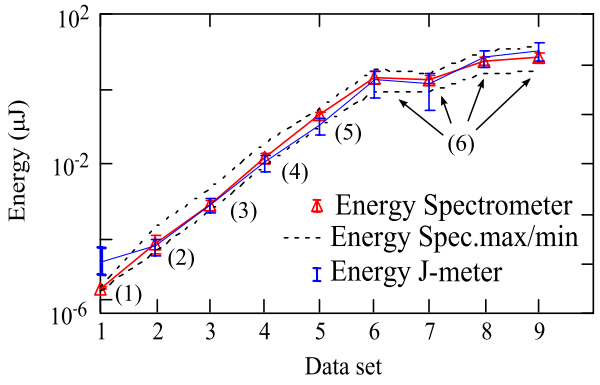

FIG. 9. Comparison of energy measured with pyroelectric detector (blue) and integrating the spectral images with the appropriate calibration factor (red). Error bars (red) correspond to 1 standard deviation over 100 shots. Numbers in parentheses indicate, for each data set, the undulator sections set at resonance.

has been obtained by varying the number of undulator sections participating in amplification.

IV. SASE EXPERIMENTS

When the beam with the parameters listed in Table I was injected in the SPARC undulator, FEL saturation was nearly reached at a resonant wavelength of $\lambda_0 = \lambda_u(1 + K_u^2/2)/(2\gamma^2) \simeq 500$ nm, where γ is the Lorentz factor. The normalized undulator strength $K_u = e_0 B_u \lambda_u/(2\pi m_0 c)$ was 2.07. We determined the overall undulator focusing by imposing a periodic condition to the transverse beam Twiss parameters over the focusing defocusing (FODO) lattice composed by an undulator section and the drift between two adjacent undulators hosting the quadrupole, and by equalizing the transverse average Twiss $\beta_{x,y}$ coefficients in the two directions (see Fig. 10). With this condition, we have $\langle\beta_x\rangle = \langle\beta_y\rangle \simeq 1.5$ m and the rms beam radius averaged over the length of the undulator section is about 120 μm.

The evolution of the radiation pulse energy as a function of the position in the undulator sequence was obtained by turning off the FEL interaction via progressively opening the gap of the sections. The pulse energy measured at the fundamental and third harmonic wavelength is shown in Fig. 11. The sequence is represented by black circles with each point corresponding to an average over 20 events. The error bars correspond to ± 2 standard deviations of the shot to shot fluctuations.

After closing all the undulator gaps to the nominal value, we optimized the output energy by varying the relative phase between the cathode drive laser and the rf acceleration fields, leading to an efficiency improvement of about 1 order of magnitude (see Fig. 11, squares). We observed an overall amplification factor close to 10^7, with an estimated gain length $L_g \simeq 0.7$ m. The effective Pierce coefficient [21], derived from the gain length according to the relation

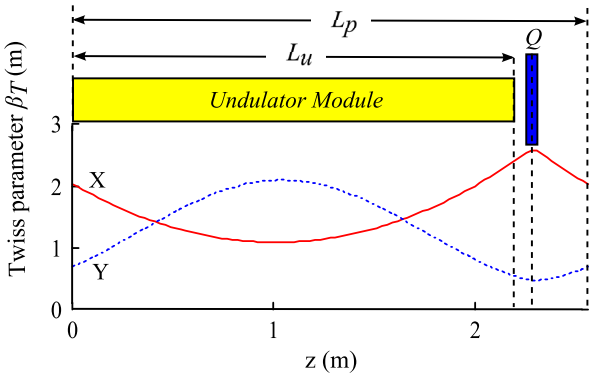

FIG. 10. Calculated evolution of the β_x (continuous red) and β_y (dotted blue) Twiss coefficients in the periodic FODO of length $L_p = 256$ cm composed by an undulator section of length $L_u = 215.6$ cm and a quadrupole (Q) in the drift between two adjacent modules.

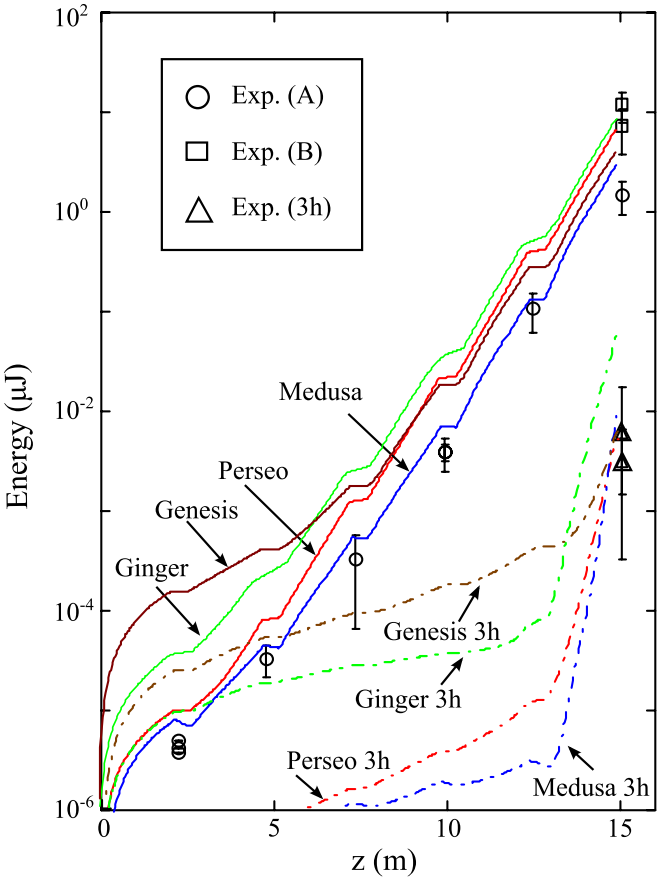

FIG. 11. Pulse energy vs longitudinal position in the undulator. Black symbols represent the measured data on the fundamental. Set (A) circles (average over 20 shots after the first undulator, $z \sim 5$ m), before optimization, set (B) squares (average over 50 shots), after optimizing laser to injector phase. Third harmonic (3h) triangles, were acquired with all the undulator gaps at resonance. Error bars represent ± 2 standard deviations of the shot to shot fluctuations (error bar is missing after the first section where the spectrum is the result of two integrations over 100 s). The lines represent simulations with PERSEO (red), GENESIS 1.3 (brown), MEDUSA (blue), and GINGER (green). The third harmonic simulation data are represented by dash-dotted lines.

$\rho = \lambda_u/(4\pi\sqrt{3}L_g)$, is $\rho \sim 1.8 \times 10^{-3}$, and may be compared with the homogeneous one-dimensional Pierce coefficient estimated from the SPARC parameters, which is $\rho \sim 3 \times 10^{-3}$. According to numerical simulations, saturation is expected at a pulse energy 0.1 mJ. The maximum energy collected was about 0.01 mJ, corresponding to about two gain lengths below full saturation. The radiation parameters after optimization are summarized in the histograms in Fig. 12, where the statistics of radiation energy, relative spectral linewidth, central wavelength, and rms spot size are shown.

The pulse energy on the fundamental and third harmonic $\lambda \sim 166$ nm has been compared with the predictions of four simulation codes: PERSEO [22] (red), GENESIS 1.3 [23]

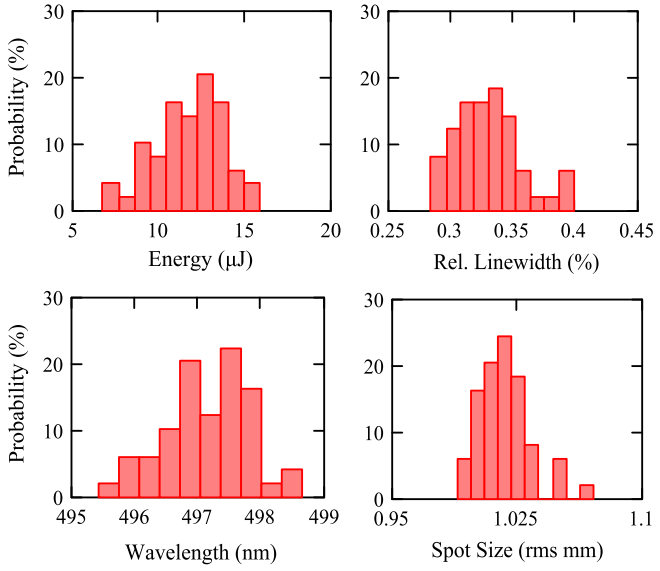

FIG. 12. Histograms of radiation pulse energy, wavelength, linewidth, and spot size at the spectrometer slit for a set of 50 events corresponding to the highest energy measured, set (B) in Fig. 11.

(brown), MEDUSA [24,25] (blue), and GINGER [26] (green) (see Fig. 11). All the calculations have been performed by assuming a beam with the longitudinal phase space corresponding to the measured data in Figs. 5 and 6, and with transverse emittance given by the quadrupole scan measurement (2.5/2.9 mm-mrad). The code PERSEO, which is a time dependent code including three-dimensional effects via a correction of the FEL coupling coefficients, has been run assuming a rms beam radius $\sigma_r = 120$ μm. In the cases simulated with all the other codes, the beam has been supposed matched to the undulator, with the Twiss parameter $\langle\beta_x\rangle = \langle\beta_y\rangle = 1.5$ m. GENESIS 1.3 and GINGER integrate three-dimensional particle equations of motion averaged over the undulator period, while MEDUSA is based on nonaveraged equations. All codes employ the slowly varying envelope approximation to Maxwell's equations. Notwithstanding the differences, all codes predict a similar gain length, and the energy values during the growth are comparable downstream from the third section. The final energy is close to the experimental value measured in the optimized case. The reason for the discrepancy after the first undulator sections may be explained considering the differences between the codes in the transverse mode representation of the field. In this regard, GENESIS 1.3 uses a Cartesian grid in (x, y), in which charge is mapped to the nearest-neighbor grid point. GINGER uses an axisymmetric grid in which charge is mapped to the nearest radial grid cells on a proportional basis and MEDUSA uses a modal decomposition for the field rather than a grid-based representation. Finally, PERSEO simulates a single transverse mode. As pointed out in a previous comparison between GINGER and GENESIS 1.3 [27], a Cartesian grid supports a much larger number high-order modes (HOMs) than is true for the other representations. These HOMs are overwhelmed by the gain in the low-order modes and become a progressively smaller component of the radiation as the interaction proceeds into the exponential regime and then to saturation. A similar argument may justify the differences on the third harmonics, where simulations made with the GENESIS 1.3 and GINGER codes show higher initial shot noise. In this regard the specific shot noise algorithm used may also introduce a difference [26,28]. Analytical estimates based on the formulas reported in Ref. [29], exploited to make the comparison with the experimental results, reproduce the full power curve vs z of either fundamental and third harmonics with a fairly satisfactory agreement, as reported in Ref. [30].

The optimization consisted in a fine-tuning of the laser to rf phase that probably compensated a phase drift which occurred after the initial beam characterization. Such a phase drift may have affected the matching condition as well as the beam emittances and correlated energy spread. We studied this effect by running PERSEO with different conditions of matching and emittances. The simulation (A) in Fig. 13 represents the matched nominal case as in Fig. 11. Simulation (B) has been obtained by increasing the beam rms radius by 30%, corresponding to $\sigma_x = 150$ μm. This simulation fits quite accurately the experimental data relevant to the not optimized sequence along the undulator. The simulation (C) corresponds to a case with nominal matching and with a reduced emittance of 2.0 mm-mrad in both planes. The slice emittance, which is the parameter affecting the FEL gain, could be lower than the value measured with the quadrupole scan and listed in Table I. In this case the effective beam size would be

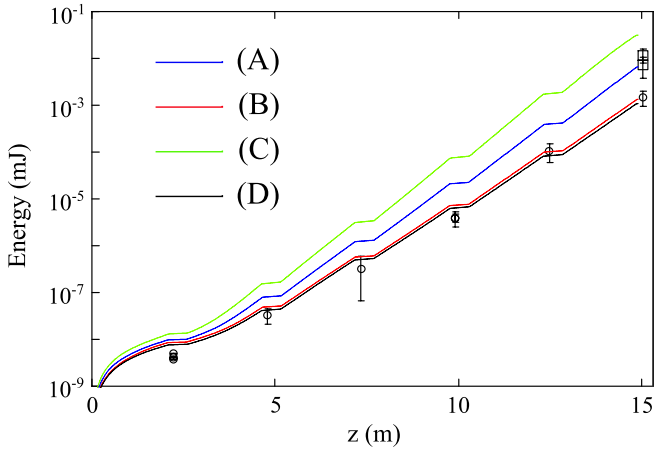

FIG. 13. Comparison between the experimental data on the fundamental harmonic (as in Fig. 11) and simulations done with PERSEO in different conditions of matching and emittances: (A) emittances (x/y) (2.5/2.9 mm-mrad) and $\sigma_r = 120$ μm; (B) emittances (x/y) (2.5/2.9 mm-mrad) and $\sigma_r = 150$ μm; (C) emittances (x/y) (2.0/2.0 mm-mrad) and $\sigma_r = 100$ μm; (D) emittances (x/y) (2.0/2.0 mm-mrad) and $\sigma_r = 150$ μm.

$\sigma_x = 100$ μm and the corresponding gain length is shorter. In this regime the gain length reduction is however mainly due to the growth of current density, rather than to the reduction of inhomogeneous broadening associated to the emittances. Simulation (D) in Fig. 13 has been obtained with the same emittance as in case (C), but with the same cross section as in (B) and fits with a similar accuracy the experimental data. We also simulated a mismatch of the beam through the undulator line in MEDUSA by making small changes in the Twiss parameters. A change in the Twiss parameters that results in an increase in the average beam envelope equal to 150 μm, yields with MEDUSA simulation results that are quite close to the experimental data.

Figure 14 shows the behavior of the radiation linewidth as a function of the longitudinal position in the undulator. The spectra are measured about two meters after the last undulator. The geometry of the vacuum chamber and the transport line to the spectrometer selects the low divergence portion of the radiation field, affecting both the measured energy and linewidth.

The lines represent predictions by PERSEO, GENESIS 1.3, MEDUSA, and GINGER. The GENESIS 1.3 calculation of the spectrum shown in the figure is given by the field at the coordinate z, propagated in the far field.

A view of the evolution of the spectrum during the exponential growth is given in Fig. 15. The spectra were acquired during a different shift than that of the previous figures, but with very similar beam parameters to those listed in Table I. The picture represents a set of six spectra obtained by progressively suppressing the amplification process in the first part of the undulator, by detuning the resonance in selected sections. This procedure allowed the measure of the spectrum generated in the remaining

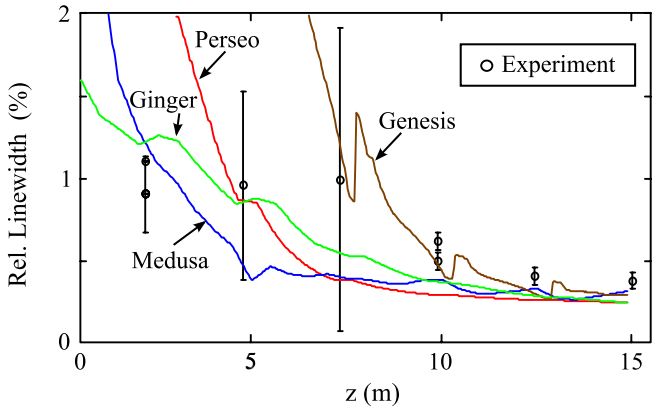

FIG. 14. Experimental linewidth of the FEL radiation (black circles) as a function of the longitudinal position in the undulator. The lines represent simulation data obtained with PERSEO (red), GENESIS 1.3 (brown), MEDUSA (blue), GINGER (green). The error bars represent ± 2 standard deviation of the measured linewidth evaluated over 50 samples.

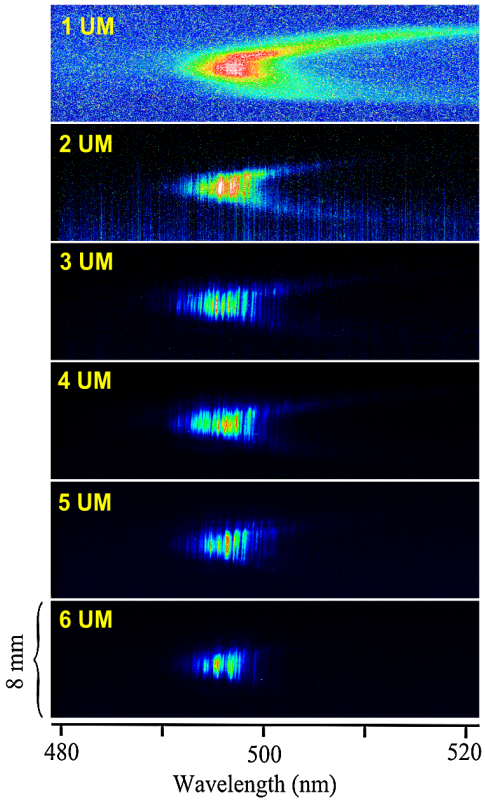

FIG. 15. Evolution of the spectrum during the exponential gain growth. The number of sections closed is reported on the upper left corner. The vertical axis in each picture indicates the position on the vertical entrance slit of the spectrometer.

modules, with an increasing number of undulators participating in amplification, while keeping unchanged the geometry of the radiation detection. The vertical axis in each picture indicates the position on the vertical entrance slit of the spectrometer. The number on the upper left corner represents the number of active undulator sections. The intensities of the different images are normalized to the peak value. The upper spectrum in Fig. 15, obtained with only the last section being resonant, is the result of an integration over 100 shots. The energy from (the last) 2–6 undulator sections allowed acquisition in single shot mode. The spiky nature of the SASE radiation is already apparent in the spectrum obtained with only two undulator sections.

V. CONCLUSIONS

In this paper we report for the first time the lasing performance obtained in SASE mode at SPARC. For a peak current of about 53 A at 500 nm wavelength, we observed an overall amplification factor close to 10^7, with an estimated gain length of 0.7 m. The maximum energy collected was about 0.01 mJ. Detailed spectra measurements were done by progressively turning off the FEL interaction in selected undulators. The evolution of the spectrum in exponential gain regime exhibits the spiky

nature of SASE, with about 20/40 longitudinal modes detected in the frequency spectrum after six undulator sections. Simulations made with the PERSEO, GENESIS 1.3, MEDUSA, and GINGER codes have been compared to the experimental data both at the fundamental and third harmonic frequency. While the agreement between predicted and observed data at the fundamental is remarkable, a fairly reasonable agreement has been also observed at the third harmonics measured at the end of the undulator.

ACKNOWLEDGMENTS

We are grateful to P. Musumeci for his contribution in the project design and in the commissioning of the SPARC photoinjector. This work has been supported by Ministero dell'Istruzione, dell'Università e della Ricerca (MIUR - DM1834 RIC.4-12-2002).

[1] A. M. Kondratenko and E. L. Saldin, Part. Accel. **10**, 207 (1980).
[2] H. Haus, IEEE J. Quantum Electron. **17**, 1427 (1981).
[3] G. Dattoli, A. Marino, A. Renieri, and F. Romanelli, IEEE J. Quantum Electron. **17**, 1371 (1981).
[4] R. Bonifacio, C. Pellegrini, and L. M. Narducci, Opt. Commun. **50**, 373 (1984).
[5] K. J. Kim, Nucl. Instrum. Methods Phys. Res., Sect. A **250**, 396 (1986).
[6] S. Milton *et al.*, Science **292**, 2037 (2001).
[7] V. Ayvazian *et al.*, Eur. Phys. J. D **20**, 149 (2002).
[8] A. Murokh *et al.*, Phys. Rev. E **67**, 066501 (2003).
[9] V. Ayvazyan *et al.*, Phys. Rev. Lett. **88**, 104802 (2002).
[10] T. Shintake *et al.*, Phys. Rev. ST Accel. Beams **12**, 070701 (2009).
[11] P. Emma *et al.*, Nat. Photon. **176**, 1038 (2010).
[12] M. Ferrario *et al.*, Phys. Rev. Lett. **99**, 234801 (2007).
[13] L. Poletto *et al.*, Rev. Sci. Instrum. **72**, 2868 (2001).
[14] L. Poletto *et al.*, Rev. Sci. Instrum. **75**, 4413 (2004).
[15] L. Serafini and M. Ferrario, AIP Conf. Proc. **581**, 87 (2001).
[16] M. Ferrario *et al.*, Phys. Rev. Lett. **104**, 054801 (2010).
[17] L. Serafini and J. B. Rosenzweig, Phys. Rev. E **55**, 7565 (1997).
[18] P. Piot, L. Carr, W. S. Graves, and H. Loos, Phys. Rev. ST Accel. Beams **6**, 033503 (2003).
[19] D. Alesini *et al.*, in Proceedings of DIPAC 2009, TUOA01, p. 146.
[20] L. Ficcadenti *et al.*, in *Proceedings of the 16th IEEE International Pulsed Power Conference, Albuquerque, NM* (IEEE, Piscataway, NJ, 2007), p. FRPMN030.
[21] J. R. Pierce, *Traveling-Wave Tubes* (Van Nostrand Company, New York, 1950).
[22] L. Giannessi, in Proceeding of the 2006 FEL Conference (2006), p. MOPPH026 [http://www.jacow.org].
[23] S. Reiche, Nucl. Instrum. Methods Phys. Res., Sect. A **429**, 243 (1999).
[24] H. P. Freund, Phys. Rev. ST Accel. Beams **8**, 110701 (2005).
[25] H. P. Freund, S. G. Biedron, and S. V. Milton, IEEE J. Quantum Electron. **36**, 275 (2000).
[26] W. Fawley, Phys. Rev. ST Accel. Beams **5**, 070701 (2002).
[27] Z. Huang and K. J. Kim, Phys. Rev. ST Accel. Beams **10**, 034801 (2007).
[28] H. P. Freund, L. Giannessi, and W. H. Miner, Jr., J. Appl. Phys. **104**, 123114 (2008).
[29] G. Dattoli, P. L. Ottaviani, and S. Pagnutti, Technical Report Booklet for FEL Design (ENEA Edizioni Scientifiche Frascati, 2007) (unpublished).
[30] G. Dattoli, P. Ottaviani, and S. Pagnutti, Technical Report No. SPARC FEL 09 006, 2009.